Check for updates

Infrared and Raman spectra of Bi₂O₂X and Bi₂OX₂ (X = S, Se, and Te) studied from first principles calculations†

Yao-Di Xu,[a] Cong Wang,[a] Yang-Yang Lv,[a] Y. B. Chen,[b] Shu-Hua Yao[acd] and Jian Zhou [ID] *[acd]

The bismuth oxychalcogenide compounds contain many different kinds of materials, such as Bi₂O₂X and Bi₂OX₂ (X = S, Se, and Te). These materials have different but similar layered crystal structures and exhibit various interesting physical properties. Here, we have theoretically investigated their Raman and infrared spectra by first principles calculations based on density functional theory. It is found that in Bi₂O₂Se the calculated frequency of the A₁g Raman active mode is in good agreement with the experimental measurements while the other three modes are ambiguous or not observed yet. The Raman and infrared spectra of other materials are also presented and need further confirmation. Our work provides the structural fingerprints of these materials, which could be helpful in identifying the crystal structures in future experiments.

1 Introduction

In recent years, bismuth oxychalcogenide materials Bi–O–X (X = S, Se, and Te) have attracted more and more attention. Among these materials, Bi₂O₂Se, synthesized more than forty years ago,[1] is one of the most studied materials and has now become a very hot topic due to its various and interesting physical properties. First, Bi₂O₂Se was suggested to be a good thermoelectric material.[2–7] In 2010, Ruleova *et al.* reported the thermoelectric properties of Bi₂O₂Se and they found that Bi₂O₂Se is an n-type semiconductor with a very low thermal conductivity and a relatively high figure of merit *ZT* about 0.2 at 800 K.[2] Several theoretical works were also conducted to explore its thermoelectric properties.[8–11] Second, Bi₂O₂Se has an ultrahigh electron mobility.[12–17] An earlier work in 2012 found that the room temperature Hall mobility of Bi₂O₂Se single crystal was on the order of 300 cm² s⁻¹ V⁻¹.[12] Recently, it was found that the low temperature (about 2 K) Hall mobility can reach more than 2.0×10^4 cm² s⁻¹ V⁻¹ in Bi₂O₂Se thin film[13–15] and 4.0×10^4 cm² s⁻¹ V⁻¹ in Bi₂O₂Se single crystal.[16] Very recently, we have

ᵃNational Laboratory of Solid State Microstructures and Department of Materials Science and Engineering, Nanjing University, Nanjing 210093, China. E-mail: zhoujian@nju.edu.cn

ᵇNational Laboratory of Solid State Microstructures and Department of Physics, Nanjing University, Nanjing 210093, China

ᶜCollaborative Innovation Center of Advanced Microstructures, Nanjing University, Nanjing, 210093, China

ᵈJiangsu Key Laboratory of Artificial Functional Materials, Nanjing University, Nanjing 210093, China

† Electronic supplementary information (ESI) available. See DOI: 10.1039/c9ra02584g

observed a superior Hall mobility of 2.2×10^5 cm² s⁻¹ V⁻¹ at 2 K in a high quality Bi₂O₂Se single crystal.[17] The high mobility in Bi₂O₂Se is possibly due to the self-modulation doping, *i.e.* the electron donor states lie above the lowest conduction band, not in the middle of the band gap.[18] Furthermore, high mobility usually induces a large magnetoresistance (MR),[19] which was also observed in Bi₂O₂Se. A longitudinal MR of about 600% (at 15 Tesla and 2 K) and 9000% (at 9 Tesla and 2 K) in Bi₂O₂Se single crystals was observed in two recent experiments.[16,17] Third, due to its high mobility and suitable band gap (about 0.8 eV), Bi₂O₂Se was used in optoelectronic devices and infrared (IR) photo-detectors.[20–22]

Bi₂O₂Te has the same crystal structure as that of Bi₂O₂Se, but it is much less studied. Luu and Vaqueiro found that Bi₂O₂Te ceramics is an n-type semiconductor with a smaller band gap (0.23 eV), electron mobility (47 cm² s⁻¹ V⁻¹ at room temperatures), and *ZT* (0.13 at 573 K), compared with those of Bi₂O₂Se.[23] The similar compound Bi₂O₂S is also less studied. Bi₂O₂S was first synthesized in 1984 and it has a different crystal structure to that of Bi₂O₂Se.[24] There are only a few studies on its optical properties.[25–27] For example, it was found that Bi₂O₂S has an indirect band gap of 1.12 eV and it is an excellent photoelectric material.[27]

On the other hand, there is another kind of bismuth oxychalcogenides Bi₂OX₂ (X = S, Se, and Te), which all share the same tetragonal lattice system. Among them, Bi₂OS₂ has been experimentally synthesized recently and it was a candidate as an optoelectronic material in the near-IR region.[28] First principles calculations indicated that the two-dimensional Bi₂OS₂ nanosheet possesses a direct band gap and an ultrahigh electron mobility (up to 2.6×10^4 cm² s⁻¹ V⁻¹).[29] To the best of our knowledge, Bi₂OSe₂ and Bi₂OTe₂ have not been synthesized

experimentally. However, first principles calculations showed that they have the same crystal structure as that of Bi_2OS_2.[30] In particular, the calculated electron and hole effective mass of Bi_2OX_2 is very small. For example, the effective mass of Bi_2OTe_2 is only 0.02 and 0.012 for electron and hole.[30] Another theoretical study indicated that Bi_2OX_2 materials show promising characteristics in applications for solar cells and thermoelectric devices.[31]

Besides Bi_2O_2X and Bi_2OX_2, the first BiS_2 family superconductor $Bi_4O_4S_3$ was studied over the past few years.[32,33] Later, it was found that $Bi_4O_4S_3$ is a mixture of the two phases, Bi_2OS_2 and $Bi_3O_2S_3$.[34] The former is non-superconducting, while the latter is superconducting.[34–36]

Therefore, we can see that the Bi–O–X system contains many kinds of materials with various interesting physical properties. From the experimental point of view, it is of course very important to identify the structure of the grown crystal from the many similar Bi–O–X materials. In this regard, Raman and IR spectra are convenient and powerful methods to provide structural fingerprints of materials. However, we find that the Raman and IR studies of these materials are quite lacking. Only a few works about the Raman spectra of Bi_2O_2Se and Bi_2O_2Te have been reported until now.[14,16,37,38] For this reason, we have systematically calculated the phonon, irreducible representations, Raman and IR spectra, vibrational eigenvectors of optical phonons, and polarized Raman configurations of six materials: Bi_2O_2X and Bi_2OX_2. We mainly present the results of Bi_2O_2Se and Bi_2O_2Te since they can be compared with other works. The Raman and IR spectra of the other four materials are also given briefly and could be referenced by future experiments.

2 Computational details

The vibrational properties of Bi_2O_2X and Bi_2OX_2 (X = S, Se, and Te) are calculated by density functional theory (DFT) implemented in the Vienna *ab initio* simulation package (VASP).[39,40] The projected augmented wave method[41,42] and the generalized gradient approximation with the Perdew–Burke–Ernzerhof exchange–correlation functional[43] are used. The DFT-D3 method[44,45] is used to correct the van der Waals interactions in these layered materials. The plane-wave cutoff energy is 520 eV for all materials. Both the internal atomic positions and the lattice constants are allowed to relax until the maximal residual Hellmann–Feynman forces on atoms are smaller than 0.002 eV Å^{-1}. The k-mesh is $8 \times 8 \times 2$ for Bi_2O_2S and Bi_2OX_2 and $8 \times 8 \times 8$ for Bi_2O_2Se and Bi_2O_2Te. The Phonopy package[46] is used to calculate the phonon frequencies, eigenvectors and irreducible representations of the materials. The crystal structures and eigenvectors are plotted by the VESTA program.[47]

The IR and Raman activity of phonon modes can be analyzed by their irreducible representations. However their intensities need additional calculations. The IR intensity of a phonon mode is given by the corresponding oscillator strength:[48]

$$f(\nu) = \sum_{\alpha} \left| \sum_{s\beta} Z^*_{\alpha\beta}(s) e_{\beta}(s,\nu) \right|^2$$

where the $e_{\beta}(s,\nu)$ is the normalized vibrational eigenvector of the νth phonon mode of the sth atom in the unit cell. α and β are the Cartesian coordinates: x,y,z. $Z^*_{\alpha\beta}(s)$ is the Born effective charge tensor of the sth atom. The Born effective charge tensor and the phonon eigenvectors are calculated by the density functional perturbation theory (DFPT) implemented in the VASP code. This method has been applied to different material systems.[48–51]

The off-resonance Raman intensity of a phonon mode can be estimated by calculating the derivative of the macroscopic dielectric tensor with respect to the normal mode coordinate:[52]

$$I_{\text{Raman}}(\nu) \propto \frac{\partial \varepsilon^{\infty}}{\partial Q(\nu)}$$

where the ε^{∞} is the macroscopic high-frequency dielectric constant and $Q(\nu)$ is the normal mode coordinate of the νth phonon mode. In practice, the derivative is replaced by the central difference based on the macroscopic dielectric matrix evaluated at positive and negative displacement along the phonon mode $Q(\nu)$. The macroscopic dielectric matrix is also calculated by the DFPT method in the VASP code. This method has also been applied to different material systems.[53,54]

3 Results and discussions

3.1 Crystal structures of Bi_2O_2X and Bi_2OX_2

The six materials Bi_2O_2X and Bi_2OX_2 (X = S, Se, and Te) have three different crystal structures. Bi_2O_2S belongs to a primitive orthorhombic lattice with a space group *Pnnm* (no. 58),[24] while Bi_2O_2Se and Bi_2O_2Te possess a body centered tetragonal lattice with a space group *I4/mmm* (no. 139).[1,13,23] On the other hand, Bi_2OX_2 have a primitive tetragonal lattice with a space group *P4/nmm* (no. 129).[28,55] All the materials show layered structures as shown in Fig. 1. Bi_2O_2X consists of two Bi_2O_2 and two X layers, while Bi_2OX_2 is composed of one Bi_2O_2 and two BiX_2 layers in a unit cell. Although the symmetries of Bi_2O_2S and Bi_2O_2Se are totally different, the structure of Bi_2O_2S is a slightly distorted form of Bi_2O_2Se.[24] Therefore, the difference between the two structures shown in Fig. 1(a) and (b) is hardly visible to the naked eye. All the structures shown in Fig. 1 contain ten atoms in the unit cell. However, Bi_2O_2Se and Bi_2O_2Te shown in
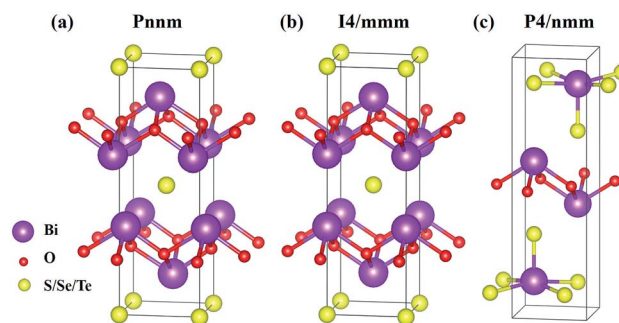
Fig. 1 Layered crystal structures of (a) orthorhombic Bi_2O_2S, (b) tetragonal Bi_2O_2Se and Bi_2O_2Te, (c) tetragonal Bi_2OS_2, Bi_2OSe_2, and Bi_2OTe_2. The purple, red, and yellow balls represent Bi, O, and S/Se/Te atoms respectively.

Table 1 Calculated lattice constants of Bi_2O_2X and Bi_2OX_2 (X = S, Se, and Te) in the unit of Å. Other theoretical and experimental results are also given for comparison

Symmetry	Material	Reference	a	b	c
Orthorhombic *Pnnm*	Bi_2O_2S	This work	3.837	3.848	11.94
		Experiment[24]	3.840	3.874	11.92
		Theory[30]	3.87	3.89	11.99
Tetragonal *I4/mmm*	Bi_2O_2Se	This work	3.891	3.891	12.20
		Experiment[1]	3.891	3.891	12.21
		Experiment[13]	3.88	3.88	12.16
		Theory[30]	3.91	3.91	12.38
	Bi_2O_2Te	This work	3.984	3.984	12.65
		Experiment[23]	3.980	3.980	12.70
		Theory[30]	4.01	4.01	12.63
Tetragonal *P4/nmm*	Bi_2OS_2	This work	3.950	3.950	13.84
		Experiment[28]	3.961	3.961	13.80
		Experiment[55]	3.964	3.964	13.83
		Theory[30]	3.96	3.96	13.69
	Bi_2OSe_2	This work	4.044	4.044	14.56
		Theory[30]	4.05	4.05	14.46
	Bi_2OTe_2	This work	4.193	4.193	15.81
		Theory[30]	4.17	4.17	15.99

Fig. 1(b) is a conventional cell, which in fact contains two primitive cells.

It is noted that among the six materials, to the best of our knowledge, Bi_2OSe_2 and Bi_2OTe_2 have not been synthesized experimentally. Their crystal structures are predicted to be the same as that of Bi_2OS_2 by first principles calculations.[30]

The calculated lattice constants in this work with the DFT-D3 correction are listed in Table 1. It is obvious that our calculated results are well consistent with the experimental measurements with the largest difference less than 1%. Our results are also in good agreement with other theoretical work.[30]

With the optimized structures, the zone-centered phonon modes, irreducible representations, IR and Raman spectra of the six materials are calculated. In the following subsections, we first present the detailed results of Bi_2O_2Se and Bi_2O_2Te since both materials have the same crystal structure and the Raman spectrum of Bi_2O_2Se is better studied than other materials. Then the brief results of Bi_2O_2S and Bi_2OX_2 are also given.

3.2 *I4/mmm* tetragonal Bi_2O_2Se and Bi_2O_2Te

The calculated zone-centered optical phonon frequencies of Bi_2O_2Se and Bi_2O_2Te are listed in Table 2. The highest phonon frequency of Bi_2O_2Se is about 433.3 cm^{-1}, while it is only 396.1 cm^{-1} in Bi_2O_2Te due to the heavier atom mass. Bi_2O_2Se and Bi_2O_2Te have the same space group of *I4/mmm* (point group D_{4h}), and their irreducible representations at the Γ point in the Brillouin zone are:

$$\Gamma_{acoustic} = E_u + A_{2u}$$

$$\Gamma_{optic} = 2E_u + 2A_{2u} + 2E_g + A_{1g} + B_{1g}$$

There are five atoms in the primitive cell of Bi_2O_2Se, therefore we can find three acoustic and twelve optical modes. These irreducible representations are also assigned to each optical phonon mode as shown in Table 2. According to the character table of the D_{4h} point group, the E_u and A_{2u} modes are IR active, while the E_g, A_{1g}, and B_{1g} modes are Raman active in Bi_2O_2Se and Bi_2O_2Te. Therefore, both materials have four Raman active (two double degenerated E_g mode and two non-degenerated A_{1g} and B_{1g} modes) and four IR active modes (two double degenerated E_u modes and two non-degenerated A_{2u} modes), as indicated in Table 2.

Recently, there have been two joint experimental and theoretical works by Pereira *et al.*[37] and Cheng *et al.*,[38] in which the phonon frequencies of Bi_2O_2Se and Bi_2O_2Te are also calculated. We listed their data in Table 2 for comparison. It is found that most of the calculated frequencies are in good agreement with ours, except for the two high-frequency IR active modes (E_u and A_{2u}) in Bi_2O_2Se, which have a maximal discrepancy of about 25 cm^{-1}. Phonon frequencies depend on the second derivative of the total energy, therefore the accuracy of the phonon calculation is usually not as good as the ones of the total energy calculations. Many parameters, such as the exchange–correlation functional, will affect the theoretical phonon frequencies. Therefore, we think such differences between these works are acceptable in phonon calculations.

We also illustrate the vibrational eigenvectors of Bi_2O_2Se in Fig. 2. It is found that the two low-frequency Raman active modes (E_g and A_{1g}) are related to the in-plane and out-of-plane

Table 2 Calculated frequencies and Mulliken symbols of zone-centered optical phonon modes of Bi_2O_2Se and Bi_2O_2Te. The theoretical frequencies in other works by Pereira[37] and Cheng[38] are also listed for comparison. Raman or IR activity of each mode is also indicated by "Raman" and "IR". The unit of the phonon frequency is cm^{-1}

Symmetry	Bi_2O_2Se			Bi_2O_2Te		Activity
	This work	Pereira[37]	Cheng[38]	This work	Cheng[38]	
E_u	54.8	59.2		56.4		IR
A_{2u}	65.0	64.5		63.3		IR
E_g	67.3	72.0	67.99	69.1	67.01	Raman
A_{1g}	162.9	165.7	159.89	150.4	147.48	Raman
E_u	268.0	293.9		243.6		IR
B_{1g}	354.3	369.4	364.02	336.0	340.33	Raman
A_{2u}	377.8	402.8		347.3		IR
E_g	433.3	444.0	428.68	396.1	386.15	Raman

E$_u$ (54.8)   A$_{2u}$ (65.0)   E$_g$ (67.3)   A$_{1g}$ (162.9)

E$_u$ (268.0)   B$_{1g}$ (354.3)   A$_{2u}$ (377.8)   E$_g$ (433.3)

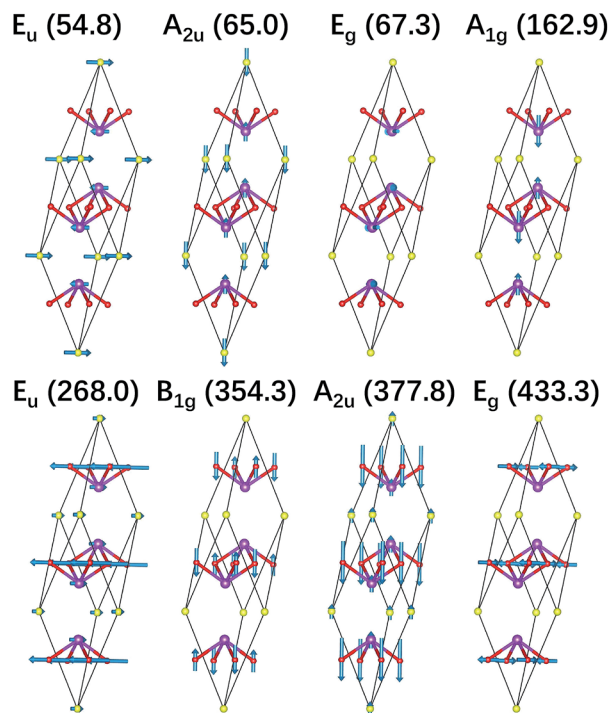**Fig. 2** Vibrational eigenvectors of the zone-centered optical phonon modes shown in the primitive cell of Bi$_2$O$_2$Se. The purple, red, and yellow balls represent Bi, O, and Se atoms respectively.

Table 3 The right angle and back scattering geometries in the polarized configurations of Raman active modes of Bi$_2$O$_2$Se and Bi$_2$O$_2$Te. The modes that can be observed in the configuration are indicated by the mark ✓

Configurations	A$_{1g}$	B$_{1g}$	E$_g$
$X(YY)Z$	✓	✓	
$Z(XX)Y$	✓	✓	
$X(ZZ)Y$	✓		
$X(YZ)Y$			✓
$Z(XZ)X$			✓
$-Z(XX)Z$	✓	✓	
$-Y(XX)Y$	✓	✓	
$-X(ZZ)X$	✓		
$-X(YZ)X$			✓

vibrations of Bi atoms, respectively. While the two high-frequency Raman active modes (B$_{1g}$ and E$_g$) represent the out-of-plane and in-plane vibrations of O atoms, respectively. Vibrations of Se atoms are not involved in any Raman active modes. The two low-frequency IR active modes (E$_u$ and A$_{2u}$) are related to the in-plane and out-of-plane vibrations of Bi and Se atoms, respectively. While the two high-frequency IR active modes (E$_u$ and A$_{2u}$) mainly represent the in-plane and out-of-plane vibrations of O atoms, respectively. The vibrational eigenvectors of Bi$_2$O$_2$Te are similar to those of Bi$_2$O$_2$Se, which are not shown here.

Then we present a detailed analysis about the polarized configurations for the Raman active modes of Bi$_2$O$_2$Se and Bi$_2$O$_2$Te. The Raman tensors of the D_{4h} point group can be written as:

$$P(\mathrm{E_g}) = \begin{pmatrix} 0 & 0 & 0 \\ 0 & 0 & e \\ 0 & e & 0 \end{pmatrix}, \begin{pmatrix} 0 & 0 & -e \\ 0 & 0 & 0 \\ -e & 0 & 0 \end{pmatrix}$$

$$P(\mathrm{A_{1g}}) = \begin{pmatrix} a & 0 & 0 \\ 0 & a & 0 \\ 0 & 0 & b \end{pmatrix} \quad P(\mathrm{B_{1g}}) = \begin{pmatrix} c & 0 & 0 \\ 0 & -c & 0 \\ 0 & 0 & 0 \end{pmatrix}$$

Qualitatively, the Raman intensity I of a phonon mode can be calculated by the formula $I \propto |e_i \cdot P \cdot e_s|^2$, where e_i and e_s are polarization directions of the incident and scattered light and P is the Raman tensor given above. In Table 3, we present the non-equivalent polarized configurations for the Raman active modes

of Bi$_2$O$_2$Se and Bi$_2$O$_2$Te. In the configuration notation $A(BC)D$, A and D represent the propagation directions of the incident and scattered light respectively, while B and C represent the polarization directions of the incident and scattered light respectively. In the right angle scattering geometry, the propagation directions of the incident and scattered light are orthogonal (first five configurations in Table 3). In the back scattering geometry, the propagation directions of the incident and scattered light are anti-parallel (last four configurations in Table 3).

From Table 3, it is interesting to find that the E$_g$ mode cannot be observed with the A$_{1g}$ and B$_{1g}$ ones simultaneously under the same polarized configuration. Also, only one A$_{1g}$ mode can be observed in the polarized configurations: $X(ZZ)Y$ or $-X(ZZ)X$. Therefore, all of the Raman active modes can be well identified under different polarized configurations. Of course, in this case, the frequencies of the four Raman active modes in Bi$_2$O$_2$Se and Bi$_2$O$_2$Te are well separated and therefore it is quite easy to identify these modes in experiments according to their frequencies without considering their polarized configurations.

IR and Raman intensities of Bi$_2$O$_2$Se and Bi$_2$O$_2$Te are also calculated directly by first principles calculations based on the
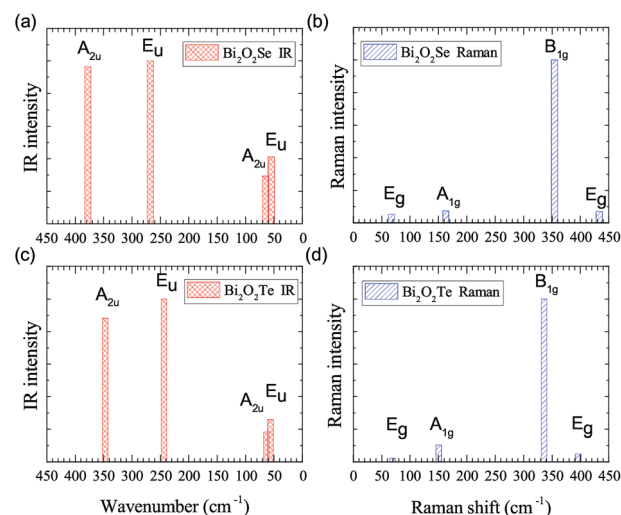
Fig. 3 Calculated IR and Raman intensities (arbitrary unit) of Bi$_2$O$_2$Se and Bi$_2$O$_2$Te.

Table 4 Comparison between calculated and experimental Raman frequencies of Bi_2O_2Se

	Raman frequency (cm^{-1})
This work	67.3 (E_g), 162.9 (A_{1g}), 354.3 (B_{1g}), 433.3 (E_g)
Experiment[14]	100, 159
Experiment[16]	84/90 (E_g^2), 159 (A_{1g})
Experiment[37]	159.2 (A_{1g})
Experiment[38]	160 (A_{1g})

equations in Section II, which are shown in Fig. 3. From Fig. 3(a) and (c), we can see that the two high-frequency IR active modes (E_u and A_{2u}) have relatively higher intensities than those of the low-frequency modes (E_u and A_{2u}). On the other hand, in Fig. 3(b) and (d), the Raman active mode B_{1g} has the highest intensity for both materials, while the other three modes have much lower intensities.

Recently, there have been four experimental works,[14,16,37,38] in which the Raman spectrum of Bi_2O_2Se was given. Wu *et al.* have synthesized the atomically thin two-dimensional and the bulk Bi_2O_2Se crystals and they observed two Raman peaks located at about 100 and 159 cm^{-1}.[14] Tong *et al.* have grown high-quality Bi_2O_2Se single crystals and found two main Raman peaks located at around 90 and 159 cm^{-1}, which are associated with the symmetries of E_g^2 and A_{1g}^2 respectively.[16] However, it seems that the E_g^2 mode in their Figure is made up of two adjacent peaks located at 84 and 90 cm^{-1}.[16] Pereira *et al.* studied the physical properties of Bi_2O_2Se at high pressure, in which they only observed one most intense Raman peak at around 159.2 cm^{-1} at room pressure.[37] The theoretical low-frequency E_g mode (near 70 cm^{-1}) can only be observed at high pressure.[37] Cheng *et al.* have measured the Raman spectra of Bi_2O_2Se and Bi_2O_2Te.[38] These results are summarized in Table 4, from which we can see that the Raman active mode A_{1g} at about 160 cm^{-1} can be well confirmed, while the E_g mode below 100 cm^{-1} is ambiguous. The discrepancy of the low-frequency E_g modes in the two experiments[14,16] is more than 10 cm^{-1}, and meanwhile both observed frequencies of the E_g modes are about 20–30 cm^{-1} higher than the theoretical result. Furthermore, the two high-frequency Raman active modes (B_{1g} and E_g) have not been observed in all the experiments[14,16,37,38] in spite of the high intensity of the B_{1g} mode in our calculations. The possible reason is due to the phonon damping caused by the large carrier concentration in Bi_2O_2Se, as indicated in Pereira's work.[37]

The Raman spectrum of Bi_2O_2Te was also measured in Cheng's work,[38] which is listed in Table 5. The two observed Raman modes (A_{1g} and B_{1g}) are well consistent with our calculations. However, the two E_g modes are not observed in

their work. It is interesting to point out that the missing B_{1g} mode in Bi_2O_2Se was observed in Bi_2O_2Te, although in a relatively low intensity compared to that of the A_{1g} mode. Therefore, the Raman spectra of Bi_2O_2Se and Bi_2O_2Te need further investigations. For example, one could try to measure the Raman spectrum of Bi_2O_2Se with a lower carrier concentration by doping or at low temperatures in a proper Raman polarized configuration.

3.3 *Pnnm* orthorhombic Bi_2O_2S

Although Bi_2O_2S has a very similar crystal structure to the one of Bi_2O_2Se shown in Fig. 1(a) and (b), they have a different symmetry. In fact, Bi_2O_2S has an orthorhombic crystal structure with a space group of *Pnnm* (point group D_{2h}). There are ten atoms in the unit cell of Bi_2O_2S resulting in thirty phonon modes. Its irreducible representations at the Γ point are presented as follows:

$$\Gamma_{acoustic} = B_{1u} + B_{2u} + B_{3u}$$

$$\Gamma_{optic} = 3A_u + 2B_{1u} + 5B_{2u} + 5B_{3u} + 4A_g + 4B_{1g} + 2B_{2g} + 2B_{3g}$$

The calculated zone-centered optical phonon frequencies of Bi_2O_2S and their symmetries are listed in Table 6. It is found that all of the modes are non-degenerate. According to the character table of the D_{2h} point group, the B_{1u}, B_{2u}, and B_{3u} modes are IR active, while the A_g, B_{1g}, B_{2g} and B_{3g} modes are Raman active. The A_u modes are neither IR nor Raman active. From our calculation, Bi_2O_2S should have twelve Raman and twelve IR active modes, as shown in Table 6.

The vibrational eigenvectors of all the zone-centered optical modes and the polarized configurations of the Raman active modes are shown in Fig. S1 and Tables S1 and S2 in the ESI.†

IR and Raman intensities of Bi_2O_2S are also calculated directly by first principles calculations, which are shown in Fig. 4. It is found that the IR modes near 60, 290 and 400 cm^{-1} have the highest intensities. In the Raman spectrum, the three

Table 5 Comparison between calculated and experimental Raman frequencies of Bi_2O_2Te

	Raman frequency (cm^{-1})
This work	69.1 (E_g), 147.48 (A_{1g}), 336.0 (B_{1g}), 396.1 (E_g)
Experiment[38]	147 (A_{1g}), 340 (B_{1g})

Table 6 Mulliken symbols and frequencies of zone-centered optical phonon modes of Bi_2O_2S. Raman or IR activity of each mode is also indicated by "Raman" and "IR". The A_u mode is neither Raman nor IR active. The unit of the phonon frequency is cm^{-1}

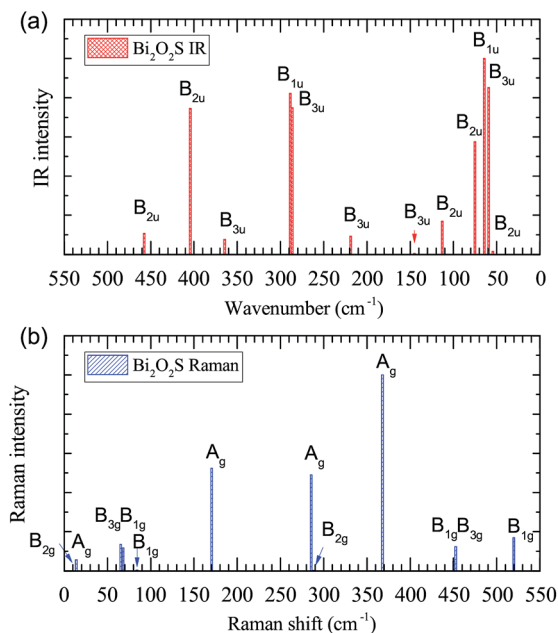| Symmetry	Bi_2O_2S	Activity	Symmetry	Bi_2O_2S	Activity
B_{2g}	9.5	Raman	B_{3u}	218.8	IR
A_g	13.9	Raman	A_g	285.2	Raman
A_u	53.7		B_{3u}	286.3	IR
B_{2u}	54.9	IR	B_{2g}	287.7	Raman
B_{3u}	60.7	IR	B_{1u}	288.5	IR
B_{1u}	64.9	IR	B_{3u}	364.4	IR
B_{3g}	65.2	Raman	A_g	367.8	Raman
B_{1g}	67.9	Raman	B_{2u}	404.2	IR
B_{2u}	75.7	IR	A_u	448.9	
B_{1g}	83.0	Raman	B_{1g}	450.6	Raman
A_u	113.1		B_{3g}	452.4	Raman
B_{2u}	113.4	IR	B_{2u}	457.5	IR
B_{3u}	144.7	IR	B_{1g}	519.1	Raman
A_g	170.6	Raman			

Fig. 4 Calculated IR and Raman intensities (arbitrary unit) of ortho-rhombic Bi_2O_2S.

A_g modes near 170, 285, and 370 cm^{-1} have the highest intensities.

It is noted that Bi_2O_2S has been synthesized in experiments,[24–26] however no Raman spectrum was measured yet. Recently, Cheng *et al.* have also calculated the Raman spectrum of Bi_2O_2S by the density functional perturbation theory in the local density approximation and norm-conserving pseudopotentials implemented in Quantum Espresso (QE) software.[38] We listed their data in Table 7 as well as ours for comparison. From the frequency perspective, we can see that the two calculations are in general consistent with each other. For example, in both works, there are five Raman modes below 100 cm^{-1}, one mode between 100–200 cm^{-1}, two modes between 200–300 cm^{-1}, and *etc.* Although the largest difference in a B_{1g} mode reaches 43 cm^{-1} (about 10%), we still think it is acceptable since the two works use totally different methods in their calculations.

However, we noted that the Mulliken symbols in the two works are quite different. In particular, the four A_g modes in Cheng's work are all below 200 cm^{-1}, while we have two A_g modes below 200 cm^{-1} and two other ones above 200 cm^{-1}. The highest A_g mode in our work is more than 210 cm^{-1} higher than theirs. This cannot be explained by the inaccuracy of the phonon frequency induced by the different parameters. It is possibly due to the different classification of the Mulliken

symbols. In the D_{2h} point group, the assignment of B_{1g}, B_{2g}, and B_{3g} depends on the three mutually perpendicular 2-fold axes along the z, y, and x directions.[56] We have tested that QE software will give different Mulliken symbols (B_{1g}, B_{2g}, and B_{3g}) depending on the orientations of the orthorhombic unit cell of Bi_2O_2S. However, the assignment of the A_g mode should be unambiguous, which is independent of the directions of the unit cell. Therefore, we think the discrepancy of the A_g Raman modes in our work and Cheng's work needs further investigations.

3.4 $P4/nmm$ tetragonal Bi_2OS_2, Bi_2OSe_2, and Bi_2OTe_2

In experiment, Bi_2OS_2 has a space group of $P4/mmm$ (point group D_{4h}).[28,55] However, to the best of our knowledge, Bi_2OSe_2 and Bi_2OTe_2 have not been synthesized in experiment. First principles calculations indicate that they share the same crystal structure as Bi_2OS_2.[30] There are ten atoms in the unit cell of Bi_2OX_2 (X = S, Se, and Te) as shown in Fig. 1(c), resulting in thirty phonon modes. The irreducible representations of Bi_2OX_2 at the Γ point are:

$$\Gamma_{acoustic} = E_u + A_{2u}$$

$$\Gamma_{optic} = 4E_u + 4A_{2u} + 5E_g + 4A_{1g} + B_{1g}$$

The zone-centered optical phonon frequencies and their symmetries of Bi_2OX_2 are listed in Table 8. The vibrational eigenvectors of Bi_2OS_2 are shown in Fig. S2 in the ESI.† The polarized configurations of the Raman spectra of Bi_2OX_2 should be the same as those of Bi_2O_2Se (Table 3) since they all belong to the D_{4h} point group.

According to the character table for the D_{4h} point group, the E_u and A_{2u} modes are IR active, while the E_g, A_{1g}, and B_{1g} modes are Raman active. Therefore, there are ten Raman active (five double degenerated E_g modes, five non-degenerated A_{1g} and B_{1g} modes) and eight IR active modes (four double degenerated E_u modes and four non-degenerated A_{2u} ones) in Bi_2OX_2.

The IR and Raman intensities of Bi_2OX_2 are also calculated directly by first principles calculations, which are shown in Fig. 5. It is found that in the IR spectrum of Bi_2OS_2, there are six modes (E_u modes around 98, 127, 262 cm^{-1} and A_{2u} modes around 129, 286, 466 cm^{-1}) which have relatively high intensities. For the Bi_2OSe_2 and Bi_2OTe_2, only four modes have high intensities. For the Raman spectra of Bi_2OS_2 and Bi_2OSe_2, there are two promising A_{1g} peaks around 132 and 346 cm^{-1} for Bi_2OS_2, and 89 and 218 cm^{-1} for Bi_2OSe_2. For Bi_2OTe_2, the A_{1g} Raman mode around 163 cm^{-1} has the highest intensity.

Table 7 Comparison between the theoretical Raman frequencies of Bi_2O_2S. For each row, the Raman modes are arranged according to their frequencies. The unit of the phonon frequency is cm^{-1}

This work	B_{2g}	A_g	B_{3g}	B_{1g}	B_{1g}	A_g	A_g	B_{2g}	A_g	B_{1g}	B_{3g}	B_{1g}
	9.5	13.9	65.2	67.9	83.0	170.6	285.2	287.7	367.8	450.6	452.4	519.1
Cheng[38]	B_{2g}	A_g	B_{2g}	A_g	A_g	A_g	B_{1g}	B_{3g}	B_{1g}	B_{1g}	B_{3g}	B_{1g}
	20.52	29.23	64.34	68.23	82.86	154.20	263.85	273.27	386.85	407.76	417.30	520.28

Table 8 Mulliken symbols and frequencies of zone-centered optical phonon modes of Bi_2OX_2 (X = S, Se and Te). Raman or IR activity of each mode is also indicated by "Raman" and "IR". The unit of the phonon frequency is cm^{-1}

Symmetry	Bi_2OS_2	Bi_2OSe_2	Bi_2OTe_2	Activity
E_u	26.0	18.8	6.5	IR
E_g	30.7	25.9	20.0	Raman
E_g	63.2	55.8	41.1	Raman
A_{2u}	63.9	54.6	50.6	IR
A_{1g}	73.2	64.1	53.5	Raman
E_u	97.7	73.2	49.2	IR
E_g	111.4	80.5	54.8	Raman
E_u	126.6	89.4	83.5	IR
A_{2u}	129.4	97.2	84.5	IR
A_{1g}	132.2	88.6	75.1	Raman
E_g	138.4	100.2	101.1	Raman
A_{1g}	149.7	138.6	123.9	Raman
E_u	262.1	228.1	183.7	IR
A_{2u}	286.0	182.3	140.9	IR
A_{1g}	346.5	217.9	163.2	Raman
B_{1g}	363.5	342.2	311.2	Raman
E_g	415.0	376.0	321.9	Raman
A_{2u}	466.0	420.0	372.1	IR

Since the tetragonal Bi_2OSe_2 and Bi_2OTe_2 have not been synthesized in experiments, we also calculated their phonon dispersion and densities of state, which are not shown here. No imaginary frequencies are found in both materials. Therefore we think the tetragonal phases of Bi_2OSe_2 and Bi_2OTe_2 are stable and they could possibly be synthesized in future experiments.
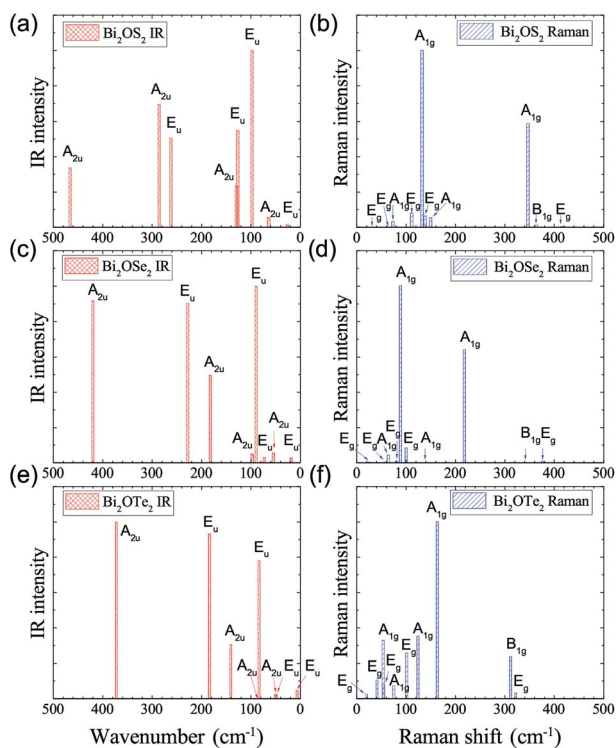

Fig. 5 Calculated IR and Raman intensities (arbitrary unit) of tetragonal Bi_2OX_2 (X = S, Se, and Te).

4 Conclusions

We have systematically calculated the Raman and infrared spectra of six Bi–O–X materials: Bi_2O_2X and Bi_2OX_2 (X = S, Se, and Te). For each material, we present their optical phonon frequencies, Raman and infrared activities and intensities, Raman polarization configurations, and vibrational eigenvectors. In particular, the Raman spectra of Bi_2O_2Se and Bi_2O_2Te are compared with the existing experimental results. In Bi_2O_2Se, only one A_{1g} Raman mode is confirmed in experiments, while the other three are ambiguous or not observed yet. In Bi_2O_2Te, both A_{1g} and B_{1g} modes are well consistent with the experiments, while two E_g modes are not observed yet. Due to the various and important physical properties in these materials, our work could be helpful in identifying the crystal structure in future experiments.

Conflicts of interest

There are no conflicts to declare.

Acknowledgements

References

1 H. Boller, *Monatsh. Chem.*, 1973, **104**, 916.
2 P. Ruleova, C. Drasar, P. Lostak, C. P. Li, S. Ballikaya and C. Uher, *Mater. Chem. Phys.*, 2010, **119**, 299.
3 K. Y. Zhang, C. G. Hu, Z. L. Kang, S. X. Wang, Y. Xi and H. Liu, *Mater. Res. Bull.*, 2013, **48**, 3968.
4 B. Zhan, Y. C. Liu, J. L. Lan, C. C. Zeng, Y. H. Lin and C. W. Nan, *Materials*, 2015, **8**, 1568.
5 X. Tan, J. L. Lan, Y. C. Liu, G. K. Ren, C. C. Zeng, Y. H. Lin and C. W. Nan, *J. Electroceram.*, 2016, **37**, 66.
6 R. Liu, J. L. Lan, X. Tan, Y. C. Liu, G. K. Ren, C. Liu, Z. F. Zhou, C. W. Nan and Y. H. Lin, *J. Eur. Ceram. Soc.*, 2018, **38**, 2742.
7 X. Tan, J. L. Lan, K. R. Hu, B. Xu, Y. C. Liu, P. Zhang, X. Z. Cao, Y. C. Zhu, W. Xu, Y. H. Lin and C. W. Nan, *J. Am. Ceram. Soc.*, 2018, **101**, 4634.
8 D. L. Guo, C. G. Hu, Y. Xi and K. Zhang, *J. Phys. Chem. C*, 2013, **117**, 21597.
9 T. V. Quang and M. Kim, *J. Appl. Phys.*, 2016, **120**, 195105.
10 M. Liangruksa, *Mater. Res. Express*, 2017, **4**, 035703.

11 C. Wang, G. Q. Ding, X. M. Wu, S. S. Wei and G. Y. Gao, *New J. Phys.*, 2018, **20**, 123014.

12 C. Drasar, P. Ruleova, L. Benes and P. Lostak, *J. Electron. Mater.*, 2012, **41**, 2317.

13 J. X. Wu, H. T. Yuan, M. M. Meng, C. Chen, Y. Sun, Z. Y. Chen, W. H. Dang, C. W. Tan, Y. J. Liu, J. B. Yin, Y. B. Zhou, S. Y. Huang, H. Q. Xu, Y. Cui, H. Y. Hwang, Z. F. Liu, Y. L. Chen, B. H. Yan and H. L. Peng, *Nat. Nanotechnol.*, 2017, **12**, 530.

14 J. X. Wu, C. W. Tan, Z. J. Tan, Y. J. Liu, J. B. Yin, W. H. Dang, M. Z. Wang and H. L. Peng, *Nano Lett.*, 2017, **17**, 3021.

15 C. Chen, M. X. Wang, J. X. Wu, H. X. Fu, H. F. Yang, Z. Tian, T. Tu, H. Peng, Y. Sun, X. Xu, J. Jiang, N. B. M. Schröter, Y. W. Li, D. Pei, S. Liu, S. A. Ekahana, H. T. Yuan, J. M. Xue, G. Li, J. F. Jia, Z. K. Liu, B. H. Yan, H. L. Peng and Y. L. Chen, *Sci. Adv.*, 2018, **4**, eaat8355.

16 T. Tong, M. Zhang, Y. Chen, Y. Li, L. Chen, J. Zhang, F. Song, X. Wang, W. Zou, Y. Xu and R. Zhang, *Appl. Phys.Lett.*, 2018, **113**, 072106.

17 Y. Y. Lv, L. Xu, S. T. Dong, Y. C. Luo, Y. Y. Zhang, Y. B. Chen, S. H. Yao, J. Zhou, Y. S. Cui, S. T. Zhang, M. H. Lu and Y. F. Chen, *Phys. Rev. B*, 2019, **99**, 195143.

18 H. X. Fu, J. X. Wu, H. L. Peng and B. H. Yan, *Phys. Rev. B*, 2018, **97**, 241203.

19 Y. Y. Lv, X. Li, J. L. Zhang, B. Pang, S. S. Chen, L. Cao, B. B. Zhang, D. J. Lin, Y. B. Chen, S. H. Yao, J. Zhou, S. T. Zhang, M. H. Lu, M. L. Tian and Y. F. Chen, *Phys. Rev. B*, 2018, **97**, 245151.

20 J. Li, Z. X. Wang, Y. Wen, J. W. Chu, L. Yin, R. Q. Cheng, L. Lei, P. He, C. Jiang, L. P. Feng and J. He, *Adv. Funct. Mater.*, 2018, **28**, 1706437.

21 J. X. Wu, Y. J. Liu, Z. J. Tan, C. W. Tan, J. B. Yin, T. R. Li, T. Tu and H. L. Peng, *Adv. Mater.*, 2017, **29**, 1704060.

22 J. Yin, Z. Tan, H. Hong, J. Wu, H. Yuan, Y. Liu, C. Chen, C. Tan, F. Yao, T. Li, Y. Chen, Z. Liu, K. Liu and H. Peng, *Nat. Commun.*, 2018, **9**, 3311.

23 S. D. N. Luu and P. Vaqueiro, *J. Solid State Chem.*, 2015, **226**, 219.

24 E. Koyama, I. Nakai and K. Nagashima, *Acta Crystallogr., Sect. B: Struct. Sci.*, 1984, **40**, 105.

25 A. L. Pacquette, H. Hagiwara, T. Ishihara and A. A. Gewirth, *J. Photochem. Photobiol., A*, 2014, **277**, 27.

26 İ. A. Kariper, *Spectrochim. Acta, Part A*, 2016, **163**, 102.

27 X. Zhang, Y. Liu, G. Zhang, Y. Wang, H. Zhang and F. Huang, *ACS Appl. Mater. Interfaces*, 2015, **7**, 4442.

28 A. Miura, Y. Mizuguchi, T. Takei, N. Kumada, E. Magome, C. Moriyoshi, Y. Kuroiwa and K. Tadanaga, *Solid State Commun.*, 2016, **227**, 19.

29 X. W. Zhang, B. Wang, X. H. Niu, Y. H. Li, Y. F. Chen and J. L. Wang, *Mater. Horiz.*, 2018, **5**, 1058.

30 X. Ma, D. Chang, C. Zhao, R. Li, X. Huang, Z. Zeng, X. Huang and Y. Jia, *J. Mater. Chem. C*, 2018, **6**, 13241.

31 S. Azam, S. A. Khan and S. Goumri-Said, *J. Electron. Mater.*, 2018, **47**, 2513.

32 S. K. Singh, A. Kumar, B. Gahtori, S. G. Sharma, S. Patnaik and V. P. S. Awana, *J. Am. Chem. Soc.*, 2012, **134**, 16504.

33 Y. Mizuguchi, H. Fujihisa, Y. Gotoh, K. Suzuki, H. Usui, K. Kuroki, S. Demura, Y. Takano, H. Izawa and O. Miura, *Phys. Rev. B: Condens. Matter Mater. Phys.*, 2012, **86**, 220510(R).

34 W. A. Phelan, D. C. Wallace, K. E. Arpino, J. R. Neilson, K. J. Livi, C. R. Seabourne, A. J. Scott and T. M. McQueen, *J. Am. Chem. Soc.*, 2013, **135**, 5372.

35 L. Li, D. Parker, P. Babkevich, L. Yang, H. M. Ronnow and A. S. Sefat, *Phys. Rev. B: Condens. Matter Mater. Phys.*, 2015, **91**, 104511.

36 J. F. Shao, Z. H. Liu, X. Yao, L. Pi, S. Tan, C. J. Zhang and Y. H. Zhang, *Phys. Status Solidi RRL*, 2014, **8**, 845.

37 A. L. J. Pereira, D. Santamaría-Pérez, J. Ruiz-Fuertes, F. J. Manjón, V. P. Cuenca-Gotor, R. Vilaplana, O. Gomis, C. Popescu, A. Muñoz, P. Rodríguez-Hernández, A. Segura, L. Gracia, A. Beltraán, P. Ruleova, C. Drasar and J. A. Sans, *J. Phys. Chem. C*, 2018, **122**, 8853.

38 T. Cheng, C. W. Tan, S. Q. Zhang, T. Tu, H. L. Peng and Z. R. Liu, *J. Phys. Chem. C*, 2018, **122**, 19970.

39 G. Kresse and J. Furthmüller, *Comput. Mater. Sci.*, 1996, **6**, 15.

40 G. Kresse and J. Furthmüller, *Phys. Rev. B: Condens. Matter Mater. Phys.*, 1996, **54**, 11169.

41 P. E. Blöchl, *Phys. Rev. B: Condens. Matter Mater. Phys.*, 1994, **50**, 17953.

42 G. Kresse and D. Joubert, *Phys. Rev. B: Condens. Matter Mater. Phys.*, 1999, **59**, 1758.

43 J. P. Perdew, K. Burke and M. Ernzerhof, *Phys. Rev. Lett.*, 1996, **77**, 3865.

44 S. Grimme, J. Antony, S. Ehrlich and H. Krieg, *J. Chem. Phys.*, 2010, **132**, 154104.

45 S. Grimme, S. Ehrlich and L. Goerigk, *J. Comput. Chem.*, 2011, **32**, 1456.

46 A. Togo and I. Tanaka, *Scr. Mater.*, 2015, **108**, 1.

47 K. Momma and F. Izumi, *J. Appl. Crystallogr.*, 2011, **44**, 1272.

48 P. Giannozzi and S. Baroni, *J. Chem. Phys.*, 1994, **100**, 8537.

49 J. Zhou and J. Dong, *J. Appl. Phys.*, 2010, **107**, 024306.

50 D. Karhánek, T. Bučko and J. Hafner, *J. Phys.: Condens. Matter*, 2010, **22**, 265006.

51 K. Esfarjani, Y. Hashi, J. Onoe, K. Takeuchi and Y. Kawazoe, *Phys. Rev. B: Condens. Matter Mater. Phys.*, 1998, **57**, 223.

52 A. Fonari and S. Stauffer, vasp_raman.py, https://github.com/raman-sc/VASP/.

53 J. M. Skelton, L. A. Burton, A. J. Jackson, F. Oba, S. C. Parker and A. Walsh, *Phys. Chem. Chem. Phys.*, 2017, **19**, 12452.

54 D. T. Larson and E. Kaxiras, *Phys. Rev. B*, 2018, **98**, 085406.

55 N. Takahashi, M. Nagao, A. Miura, S. Watauchi, K. Tadanaga, Y. Takano and I. Tanaka, *J. Ceram. Soc. Jpn.*, 2018, **126**, 591.

56 R. S. Mulliken, *J. Chem. Phys.*, 1955, **23**, 1997.